J. Astrophys. Astr. (2022) 43:93
https://doi.org/10.1007/s12036-022-09878-9

AstroSat observation of rapid type-I thermonuclear burst from low-mass X-ray binary GX 3+1

ANKUR NATH[1,2], BIPLOB SARKAR[1,*], JAYASHREE ROY[3] and RANJEEV MISRA[3]

[1]Department of Applied Sciences, Tezpur University, Napaam, Tezpur 784028, India.
[2]Faculty of Science and Technology, The ICFAI University Tripura, Agartala 799210, India.
[3]Inter-University Centre for Astronomy and Astrophysics (IUCAA), Post Bag 4, Ganeshkhind, Pune 411007, India.
*Corresponding author. E-mail: biplobs@tezu.ernet.in

MS received 10 July 2021; accepted 15 June 2022

Abstract. We report the results of an observation of low-mass X-ray binary GX 3+1 with AstroSat's large area X-ray proportional counter (LAXPC) and soft X-ray telescope (SXT) instruments on-board for the first time. We have detected type-I thermonuclear burst (∼15 s) present in the LAXPC 20 light curve with a double peak feature at higher energies and our study of the hardness–intensity diagram reveals that the source was in a soft banana state. The pre-burst emission could be described well by a thermally Comptonized model component. The burst spectra is modeled adopting a time-resolved spectroscopic method using a single color blackbody model added to the pre-burst model, to monitor the parametric changes as the burst decays. Based on our time-resolved spectroscopy, we claim that the detected burst is a photospheric radius expansion (PRE) burst. During the PRE phase, the blackbody flux is found to be approximately constant at an averaged value of ∼2.56 in 10^{-8} ergs s^{-1} cm^{-2} units. On the basis of literature survey, we infer that AstroSat/LAXPC 20 has detected a burst from GX 3+1 after more than a decade, which is also a PRE one. Utilizing the obtained burst parameters, we provide a new estimation to the source distance, which is ∼9.3 ± 0.4 kpc, calculated for an isotropic burst emission. Finally, we discuss and compare our findings with the published literature reports.

Keyword. X-rays: binaries—stars: neutron—pulsars: individual: GX 3+1—X-rays: stars—methods: data analysis—AstroSat: LAXPC/SXT.

1. Introduction

The low-mass X-ray binary (LMXB) GX 3+1 was first detected during an Aerobee-rocket flight on 16 June 1964 (Bowyer *et al.* 1965). LMXBs are binary systems which are older than $\sim 10^9$ years with their companion stars having mass $\leq 1\ M_\odot$ (Bhattacharya & van den Heuvel 1991; Verbunt 1993). Ever since the discovery of LMXBs, which have neutron stars (NS) as compact objects, short thermonuclear bursts have been reported (Belian *et al.* 1976; Grindlay *et al.* 1976; Strohmayer & Bildsten 2006; Galloway *et al.* 2020). X-ray bursts in LMXBs are marked as rapid rise in the photon count in the time scale of seconds, followed by an exponential decay (Galloway *et al.* 2008). These are the nuclear runaway phenomena, which are caused by the accreted material from the companion falling onto the NS surface via Roche-lobe overflow mechanism. Pure or mixed hydrogen burns up to a critical density, beyond which bright bursts in X-rays occur locally—see reviews by Lewin *et al.* (1993), Strohmayer & Bildsten (2006) and Bhattacharyya (2010). Usually, the decay times vary between ∼10 and 100 s as reported by Lewin (1977), Hoffman *et al.* (1978), Lewin *et al.* (1993) and Galloway *et al.* (2008). During spectral modeling, type-I bursts are normally described with blackbody models.

GX 3+1 is a persistently bright X-ray binary source. After eight years of its discovery, it was first detected with type-I short bursts, which indicated that the compact object at the center certainly has to be an NS (Makishima *et al.* 1983). As reported from the all sky monitor (ASM) observation (Levine *et al.* 1996), the average X-ray intensity of GX 3+1 is slowly varying over a time scale of months to years by a factor of ∼2 with high X-ray luminosity (10^{37}–10^{38} ergs s^{-1}) and non-periodic behavior (Mondal *et al.* 2019).

Published online: 06 December 2022

Being a luminous, persistent source GX 3+1 has been observed by many major X-ray missions, such as Ginga (Asai *et al.* 1993), EXOSAT (Schulz *et al.* 1989, RXTE (Bradt *et al.* 1993; Kuulkers & van der Klis 2000), BeppoSAX (den Hartog *et al.* 2003), INTEGRAL (Chenevez *et al.* 2006; Paizis *et al.* 2006), Chandra (van den Berg *et al.* 2014), XMM-Newton (Pintore *et al.* 2015), NuSTAR (Mondal *et al.* 2019). This present work is based on the observation of GX 3+1 by mission AstroSat.

LMXBs are mainly grouped as Z or atoll sources, based on the characteristic shapes they trace on their color–color diagrams (CCD). Atoll sources display mainly two tracks in hardness–intensity diagrams (HID): the banana and island states. GX 3+1 has been reported to be a bright atoll source having a soft spectrum typically ∼2–10 keV (Mondal *et al.* 2019). Ever since its discovery, this source has been always found in banana state. Two branch structures were detected in its HID, which were identified as lower and upper banana states in the report by Asai *et al.* (1993). No island state has been observed so far from GX 3+1 and no kHz quasi-periodic oscillations (QPOs) are detected (Homan *et al.* 1998; Oosterbroek *et al.* 2001; Chenevez *et al.* 2006; Mondal *et al.* 2019).

Historically, GX 3+1 has shown doubly peaked bursts in 9–22 keV energy band reported by Makishima *et al.* (1983), which was the first report of type-I bursts from GX 3+1. Following this, GX 3+1 was found to be a very active X-ray burster and bursts were studied by Asai *et al.* (1993); Pavlinsky *et al.* (1994) and Molkov *et al.* (1999). However, the first investigation of a double peak photospheric radius expansion (PRE) burst was carried out by Kuulkers & van der Klis (2000) using RXTE data. They had estimated the source distance to be between 4.2 and 6.4 kpc for an uncertainity of 30%. A total of 61 bursts from GX 3+1 was reported by den Hartog *et al.* (2003), which were observed in a high state of the source. However, an exceptional superburst was reported by Kuulkers (2002) with RXTE/ASM data, which had a decay time of ∼1.6 h. An unusual intermediate burst with a duration of ∼30 min was detected in 2004 by INTEGRAL/JEM-X, which was analysed by Chenevez *et al.* (2006). The same data set was re-evaluated by Alizai *et al.* (2020) using different spectral models. Thus, we found that no burst phenomenon has been reported for this source since 2004.

Thermonuclear X-ray bursts from GX 3+1 have never been reported earlier using AstroSat data. However, type-I themonuclear bursts has been detected by AstroSat previously from various LMXBs (Bhattacharyya *et al.* 2018; Beri *et al.* 2019; Bhulla *et al.* 2020; Devasia *et al.* 2021; Roy *et al.* 2021; Kashyap *et al.* 2022a). PRE burst events for the LMXB 4U 1636-536 have been reported earlier using AstroSat data by Beri *et al.* (2019) and Roy *et al.* (2021).

The spectral fitting of NS bursts involve modeling with a single color blackbody component (Hoffman *et al.* 1977; Beri *et al.* 2019; Bhulla *et al.* 2020). The pre-burst spectrum of several LMXBs are found to be well fitted with a thermally Comptonized model, which describes the powerlaw behavior of the energy (Pintore *et al.* 2015; Verdhan *et al.* 2017; Bhattacharyya *et al.* 2018; Chen *et al.* 2019). The parameter values of the black-body model could be used to estimate the temperature near the NS surface $kT_{bb} > 1$ keV (Seifina & Titarchuk 2012) and the physical radius of the NS. The model parameters evolve with time in rapid events like bursts, so it is needful to divide bursts into short time intervals and fit the spectra of each interval, from the rise to the decay of the burst, which is the conventional method of time-resolved spectroscopy (Swank *et al.* 1977; Lewin *et al.* 1993). The source's persistent pre-burst spectra is assumed to be unevolved during the burst and used to serve as the background spectrum for the burst spectra. This is the conventional method of burst spectral analysis. Since type-I bursts are highly luminous than the source's average photon count rate, so it is acceptable to consider modeling of the burst spectra distinguishably, assuming that the burst does not influence the background persistent emission. But reports have showed that bursts can modify the persistent spectra (Chen *et al.* 2012; in't Zand *et al.* 2013; Degenaar *et al.* 2018; Keek *et al.* 2018). Worpel *et al.* (2013, 2015) introduced f_a (which is a scaling factor supplied to the persistent spectrum) method and reported the change in persistent flux due to the burst. When the f_a is fixed at unity, the model follows the conventional method.

The objectives of this paper are summarized in the following: (i) reporting the detection of a type-I X-ray burst from GX 3+1 with AstroSat, (ii) reporting the detection of the double-peak feature in the burst at higher energies, and (iii) presenting spectral analysis of the burst and reporting the physical parameters, such as blackbody temperature, blackbody flux and radius of the NS photosphere.

The organization of this paper is as follows: Section 2 discusses observational details and mentions all the data reduction techniques briefly. Section 3 presents light curve, hardness ratio of the photon count rate, HID, an energy resolved burst light curve and QDP modeling of the burst at each energy band. We have performed a joint fitting of the persistent pre-burst spectrum, using SXT

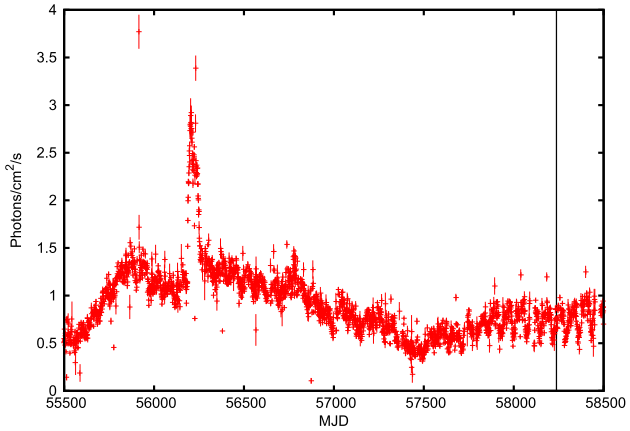

Figure 1. MAXI long time light curve for GX 3+1 in the energy band of 2–20 keV. The vertical line marks the AstroSat observation date.

and LAXPC 20 data and obtained the parameter values for a thermally Comptonized component, elaborated in Section 4.1. We have adopted the conventional approach to fit the model of the burst, elaborated in Section 4.2. All the results are discussed and compared to highlight the consistencies with earlier published reports in Section 5.

2. Observations and data reduction

AstroSat is India's first multi-wavelength astronomy mission satellite launched on 28 September 2015. For dedicated studies on X-ray astronomy, AstroSat has been provided with payloads soft X-ray focusing telescope (SXT) and three large area X-ray proportional counters (LAXPC) named as LAXPC 10, LAXPC 20 and LAXPC 30. AstroSat observed GX 3+1 in an announcement of opportunity (AO) observation conducted on 29–30 April 2018 (Obs ID: A04_122T01_9000002064). The observation was done for the right ascension (RA) $\alpha = 266.983329$ and declination point (DEC) $\delta = -26.56361$ in international celestial reference system (ICRS), for the celestial coordinates of GX 3+1. The observation by AstroSat is marked on the MAXI long time light curve in 2–20 keV shown in Figure 1. The source was showing a persistent behavior during the AstroSat observation, as it is evident from the MAXI light curve.

2.1 *AstroSat–SXT*

The SXT (Singh *et al.* 2016, 2017) has an operational energy band of 0.3–8.0 keV (Singh *et al.* 2017; Bhattacharyya *et al.* 2021). The SXT pipeline software[1] (version: AS1SXTLevel2-1.4b) is used to generate the level 2 data of nine orbits using the photon counting (PC) mode for level 1 data. The SXT event merger script is used to merge the data for different orbits to produce the clean event file. An encircled region of radius 13.5 arcmin in physical coordinates is extracted which comprises ∼96% of the source photons for the generation of source spectrum. This extraction is done using the standard tools of XSELECT V2.4g. The light curve of minimum allowed time bin for SXT instrument, i.e., 2.3775 s, is thus obtained from this region file. The auxillary response file (ARF) is generated by using sxtARFModule[2] tool of the ARF on-axis (version 20190608) provided by the SXT instrument team. The SXT spectrum file is used with a blank sky background spectrum provided by the SXT instrument team during our model fitting. No pile up is observed for the source. The energy band kept during the generation of the SXT spectrum file is the default 0.3–8.0 keV (Singh *et al.* 2017; Bhattacharyya *et al.* 2021).

2.2 *AstroSat–LAXPC*

LAXPC counters have been designed to detect X-ray photons of energies 3.0–80 keV (Yadav *et al.* 2016; Antia *et al.* 2021). Beside a total of three proportional counters as mentioned before, LAXPC has a total effective area of ∼8000 cm^2. Each of the three counters work independently to record photons with a time resolution of roughly 10 μs. This makes LAXPC able to observe fast variability like thermonuclear bursts. We use the data only from LAXPC 20 because LAXPC 10 has been found displaying instability in its response and LAXPC 30 is excluded as it has been officially shut down, at the time of observation of GX 3+1.

We have generated the level 2 data of nine orbits from LAXPC 20 using the event analysis (EA) mode. EA mode data contains the information about the time, anode ID and pulse height amplitude (PHA) for each event. The processing of the LAXPC data is done using individual routine software LaxpcSoft[3] version: 19 May 2018. We have only used the layer 1 (top layer) of the LAXPC 20 counter for the temporal and spectral analysis except for the full-time light curve, which is generated using all the layers of the same counter.

[1] http://astrosat-ssc.iucaa.in/?q=sxtData.

[2] www.tifr.res.in/~astrosat_sxt.

[3] http://astrosat-ssc.iucaa.in/?q=laxpcData.

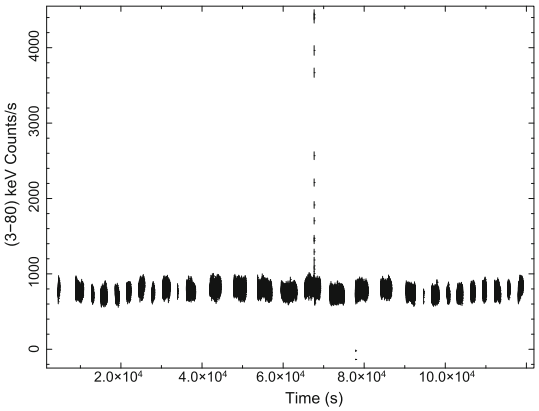

Figure 2. AstroSat/LAXPC counter 20 light curve for ∼100 ks data in the 3.0–80 keV energy band for a bin size of 1.0 s. A burst is observed at nearly 60 ks from the start of the observation with a sudden increment in the count rate by ∼4 folds of the source's persistent count rate.

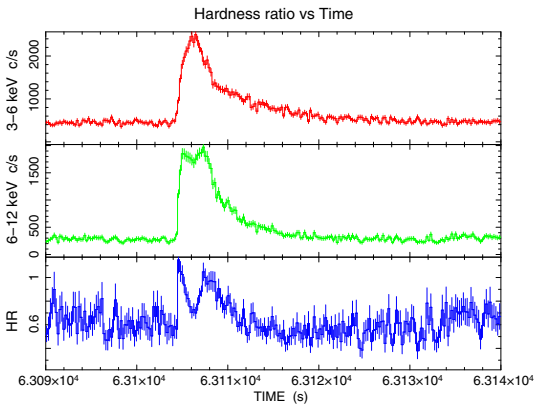

Figure 3. Upper and middle panels show source LAXPC 20 layer 1 light curves in the energy bands 3–6 and 6–12 keV, respectively. Bottom panel shows the hardness ratio HR = (6−12 keV)/(3−6 keV). The binning size is 0.2 s. An increase in HR is seen during the burst, crossing 1.

3. Temporal analysis

The LAXPC 20 light curve is generated for the good time intervals only. The background is subtracted for a default 2% systematic error. A nearly persistent photon count rate of ∼1000 counts per s is observed from the light curve. As we cross about 60 ks from the observational start time, the burst feature is prominent (Figure 2) with its photon count rate (∼4000 counts per s) almost four times the non-burst rate.

Figure 3 shows the detected photons in LAXPC 20 layer 1 in energy bands of 3–6 keV and 6–12 keV with their respective light curves plotted simultaneously and the hardness ratio (HR) (6–12 keV)/(3–6 keV) of the two light curves in the bottom panel with their corresponding hardness ratio shown at the bottom panel. The

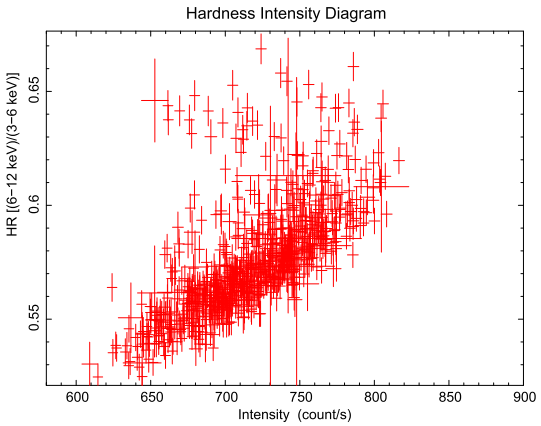

Figure 4. Hardness–intensity diagram of GX 3+1. The hardness ratio (HR) is taken as the ratio of the count rates in the energy bands of 6–12 and 3–6 keV, respectively. The HR shows a positive correlation with the intensity. The plot is generated for a bin time of 60.0 s.

bin size is selected as 0.2 s. We have used Xronos v5.22 to generate this multiplot. We can thus infer that during the entire observation period, the source is detected in a soft state since the average hardness ratio was ∼0.6–0.7 during the entire observation. But during the burst, we notice the ratio increases, crossing 1.0, followed by a sharp drop in the hardness and a subsequent rise. As the burst decays, the ratio drops to the persistent level.

The HID is plotted as a function of source's intensity (Figure 4). For an HR (6–12 keV)/(3–6 keV) with a binning size of 60 s, we observe a positive correlation of the HR with source intensity in the energy band of 3–12 keV. A positive correlation between hardness and intensity is also reported by Mondal *et al.* (2019), which indicates the characteristic soft banana state.

3.1 *Search for burst oscillations*

We have investigated the power density spectrum (PDS) to detect burst oscillations using data from LAXPC 20 all layers. To generate the PDS, we have used the Laxpcsoftware task laxpc_find_freqlag, which outputs the power spectra as a function of frequency. These PDS are generated using a burst GTI file of 16 s exposure. We have also used the GTI file for the entire orbit data from all layers of LAXPC 20 in which the burst has been detected and plotted the respective PDS up to 1000 Hz. We have also parallely used the ftool powspec 1.0 (XRONOS v 6.0) to generate PDS with binning of 0.005, 0.004, 0.003 and 0.002 s. However, we could not detect any signal of oscillations.

3.2 *Energy-resolved burst profile*

To resolve the entire burst into separate energy bands, we generate four burst light curves in narrow energy bands: 3–5, 5–8, 8–12 and 12–20 keV. All these light curves have a binning size of 0.16 s. From Figure 5, we observe that the burst has the highest photon count rate in 5–8 keV band, crossing 2000 counts per s. This is followed by the light curves in 3–5, 8–12 and 12–20 keV band in a descending order of photon count rate. The double-peak feature is observed in the 8–12 and 12–20 keV bands. These burst light curves are generated after subtracting the background light curves, using a default systematic error of 2% for the LAXPC instrument and no scaling factors are multiplied.

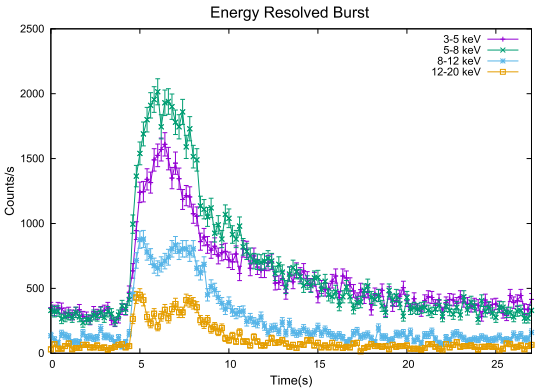

Figure 5. Plot shows the thermonuclear X-ray burst observed in different energy bands. The X-ray burst decays rapidly as energy approaches to 20 keV. The highest photon count is observed for the energy band of 5–8 keV. All the light curves have a binning size of 0.2 s.

We have performed a measurement of the exponential decay times of the burst in four energy bands by fitting the corresponding light curves with a model combination of a constant added to QDP Burs model (https://heasarc.gsfc.nasa.gov/ftools/others/qdp/qdp.html) (Devasia *et al.* 2021). To achieve a better fitting, we include two Burs models. We show the model fits for four burst profiles in their respective energy bands in Figure 6 and the obtained rise time, the approximate ratio of the burst peak count rate and the persistent count rate and the decay time are reported in Table 1. We found that the peak to persistent count rate ratio is higher for higher energy bands as evident from Figure 6(a–d). QDP Burs modeling of burst profile has been done previously by Beri *et al.* (2019), Marino *et al.* (2019) and Hu *et al.* (2020) to obtain their timing properties. The peak flux values listed

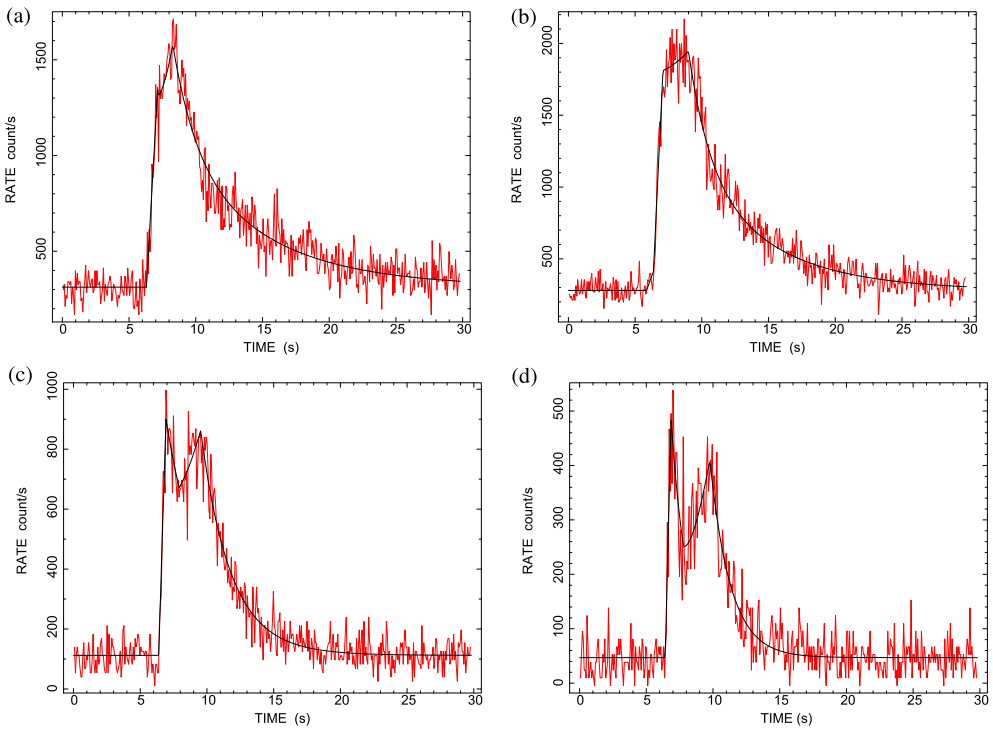

Figure 6. QDP modeling of the type-I burst. Figure shows modeling of the burst in (a) 3–5 keV, (b) 5–8 keV, (c) 8–12 keV energy ranges and (d) models the burst light curve in 12–20 keV energy range. At higher energies, the double-peaked feature is seen more distinctively.

Table 1. Duration of rise, peak to persistent count ratio, decay duration and flux at the burst peak, estimated for four narrow energy bands of the burst. The count ratio is the approximate ratio of peak count rate and the persistent count rate, obtained for each Burs model.

Energy band (keV)	Duration of rise (s)	Count ratio	Decay duration (s)	Peak flux (10^{-9} ergs s^{-1} cm^{-2})
3–5	0.845, 1.05	∼3.18, 5.12	1.7, 6.81	9.763
5–8	0.72, 3.15	∼6.96, 4.24	5.98, 1.56	11.471
8–12	0.52, 1.616	∼8.03, 7.58	2.87, 1.89	8.430
12–20	0.4, 1.97	∼10.43, 8.69	1.22, 1.59	5.270

in Table 1 have been obtained by using the XSPEC command flux on the spectral files of exposure ∼3 s near the peak of each of the energy resolved burst light curve.

4. Spectral analysis

To perform the spectral fitting, we have used the SXT spectrum file, mentioned in Section 2.1. We have considered only layer 1 data from LAXPC 20 unit to obtain non-burst or pre-burst spectrum and the burst spectrum. We consider two broad regions of data—the pre-burst region and burst region.

4.1 *Pre-burst analysis*

The pre-burst energy spectrum of the source is obtained from the combined analysis of the SXT and LAXPC 20 layer 1 spectral data of ∼841 s, which is modeled by a thermally Comptonized component NTHCOMP (Zdziarski *et al.* 1996; Życki *et al.* 1999) in XSPEC v12.10.1f (Arnaud 1996). We choose an energy range with a lower limit at 0.6 keV because of the uncertainties in the response at lower energies and higher limit at 16 keV, since the spectra is found to be background dominated at higher energies. The XSPEC routine TBABS (Wilms *et al.* 2000) is used for taking the interstellar medium (ISM) absorption into account. We freeze the neutral hydrogen column density (N_H) at 1.4×10^{22} cm^{-2} (Figure 7), which is close to the value of $\sim 1.5 \times 10^{22}$ cm^{-2} reported by Morrison and McCammon (1983). We select the input type-I, which considers that the seed photons are supplied to the corona by the accretion disk.

Table 2 shows all the parameter values achieved for the best fit. The LAXPC 20 layer 1 spectrum and the SXT spectrum are obtained for energy bands

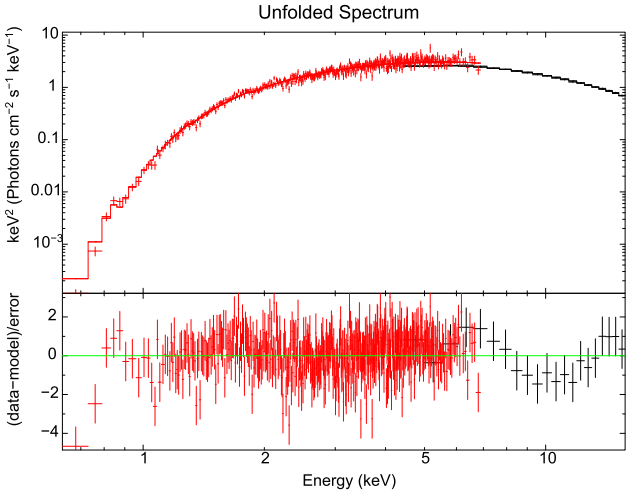

Figure 7. Unfolded spectra from AstroSat for GX 3+1 (SXT spectrum in red and LAXPC 20 layer 1 spectrum in black). The top panel shows the spectra fitted with the model constant × TBABS × NTHCOMP. The energy band used is 0.6–16.0 keV. Bottom panel shows the ratio of data and model.

4.0–16.0 and 0.6–7.0 keV, respectively. The SXT spectrum's response file is provided a gain correction with its slope frozen to 1.0 and its best fit offset obtained $\sim 0.047^{+0.008}_{-0.012}$. A systematic error of 3% is considered to account for the uncertainties in the response calibration[4] (Maqbool *et al.* 2019; Mudambi *et al.* 2020).

While fitting, the photon index Γ is found to settle at ∼3.5 ± 0.35, which is in agreement with the reported values from Chenevez *et al.* (2006); Pintore *et al.* (2015) and Ludlam *et al.* (2019). The electron temperature, kT_e obtained is $\sim 4.46^{+2.55}_{-0.88}$ keV and the seed photon temperature $kT_{\rm nth}$ achieved is $\sim 1.82^{+0.07}_{-0.07}$ keV. The low value of the electron temperature indicates the soft state of the source, which is in agreement with

[4] https://www.tifr.res.in/~astrosat_sxt/dataana_up/readme_sxt_arf_data_analysis.txt.

Table 2. Best-fit parameter values for the joint pre-burst spectral modeling of SXT and LAXPC 20 layer 1 data with a thermally Comptonized multicolor black-body constant × TBABS × NTHCOMP. Errors are at 90% confidence range for each parameter.

Component	Parameter (unit)	LAXPC 20	SXT
TBABS	$N_{\rm H}(10^{22}\ {\rm cm}^{-2})$	1.4 (frozen)	1.4 (frozen)
constant		1.0 (frozen)	$1.18^{+0.04}_{-0.04}$
NTHCOMP	Γ^{α}	$3.5^{+0.4}_{-0.3}$	$3.5^{+0.4}_{-0.3}$
	kT_e^{β} (keV)	$4.46^{+2.55}_{-0.88}$	$4.46^{+2.55}_{-0.88}$
	$kT_{\rm nth}^{\gamma}$ (keV)	$1.82^{+0.07}_{-0.07}$	$1.81^{+0.07}_{-0.07}$
	$N_{\rm nth}^{\delta}$	$0.73^{+0.04}_{-0.04}$	$0.73^{+0.04}_{-0.04}$
Gain	Slope	–	(1.0)
	Offset (E-02)	–	$5.73^{+0.006}_{-0.007}$
	χ^2/d.o.f	1.08	1.08
	f^{η} (10^{-9} ergs s^{-1} cm^{-2})	$4.46^{+0.1}_{-0.1}$	$6.41^{+0.1}_{-0.1}$

$^{\alpha}$Powerlaw photon index of NTHCOMP. $^{\beta}$Electron temperature of the corona. $^{\gamma}$Seed photon temperature of the disk. $^{\delta}$Normalization of NTHCOMP. $^{\eta}$Unabsorbed flux in the energy of 4.0–16.0 keV for LAXPC 20 and 0.6–7.0 keV for SXT data.

our obtained HID shown in Figure 4. The fit attains a chi-squared value of 471.76 for 437 degrees of freedom, which is a good fitting. The SXT spectrum is rescaled by a constant factor of $\sim 1.18^{+0.04}_{-0.04}$, while keeping the same constant fixed to 1.0 for LAXPC 20 layer 1 spectrum.

The unabsorbed flux is found to be slightly more for the SXT spectra in comparison to the LAXPC 20 layer 1 spectra (4.46 and 6.41 in units of 10^{-9} ergs s^{-1} cm^{-2}, for LAXPC and SXT, respectively), which is obtained using the convolution model CFLUX. These values are in agreement with the persistent flux reported by Pintore *et al.* (2015) and Ludlam *et al.* (2019).

We have also attempted to add a DISKBB model to the NTHCOMP, but it has resulted in an overestimation of the errors in the fit. We have also tried to fit the pre-burst spectra by selecting the input type = 0, so as to remodel the spectrum with blackbody seed photons. This has resulted in a poor fit with a reduced chi-squared value rising to ∼1.21. However, adding a BBODY model to the NTHCOMP, slightly lowered the reduced chi-squared value to ∼1.18, but the obtained normalization is found to be very small and its error limits could not be constrained.

4.2 *Burst analysis*

We investigated the evolution of the free parameters during the dominant phase of the burst by systematically

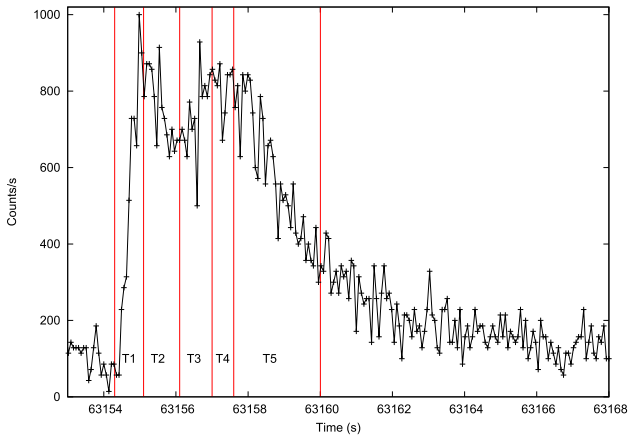

Figure 8. Time bins selected for spectroscopy. The burst light curve shown here is in 8–12 keV energy band.

dividing the burst exposure into a total of five time intervals: T1, T2, T3, T4 and T5 as shown in Figure 8. The exposure of the different time intervals are T1 = 0.8 s, T2 = 1.0 s, T3 = 0.9 s, T4 = 0.6 s and T5 = 2.4 s. We obtained the spectra for each of these five time bins from the top layer or layer 1 of the LAXPC 20. The energy band selected during XSPEC fitting is 4–16 keV. Harder energies >16 keV are ignored as the burst is observed predominantly at softer energies (Figure 5). Energies <4.0 keV are ignored to avoid uncertainties in the response from LAXPC. As the model TBABS × NTHCOMP has described the pre-burst spectra successfully, we proceed to investigate the burst by adding a blackbody model (Degenaar *et al.* 2016) BBODYRAD to

pre-burst model (Galloway *et al.* 2008; Beri *et al.* 2016). The NTHCOMP is fed with pre-burst parameter values which are kept frozen and only the blackbody parameters are set free. This conventional approach is adopted to model all the five burst spectra as shown in Figure 9. A systematic error of 2% is considered to account for the uncertainties in the spectral response of LAXPC following the works of Antia *et al.* (2017), Misra *et al.* (2017); Sreehari *et al.* (2019, 2020), Kashyap *et al.* (2022b) and Majumder *et al.* (2022).

Table 3 reports the blackbody temperature and the normalization constant achieved during the fitting. We noticed that the temperature kT_{bb} reaches a local minimum of 1.61 ± 0.08 keV corresponding to which the Norm_{bb} reaches the maximum value $= 496.05^{+138.64}_{-106.98}$. During T5, which is the decay phase of the burst, the

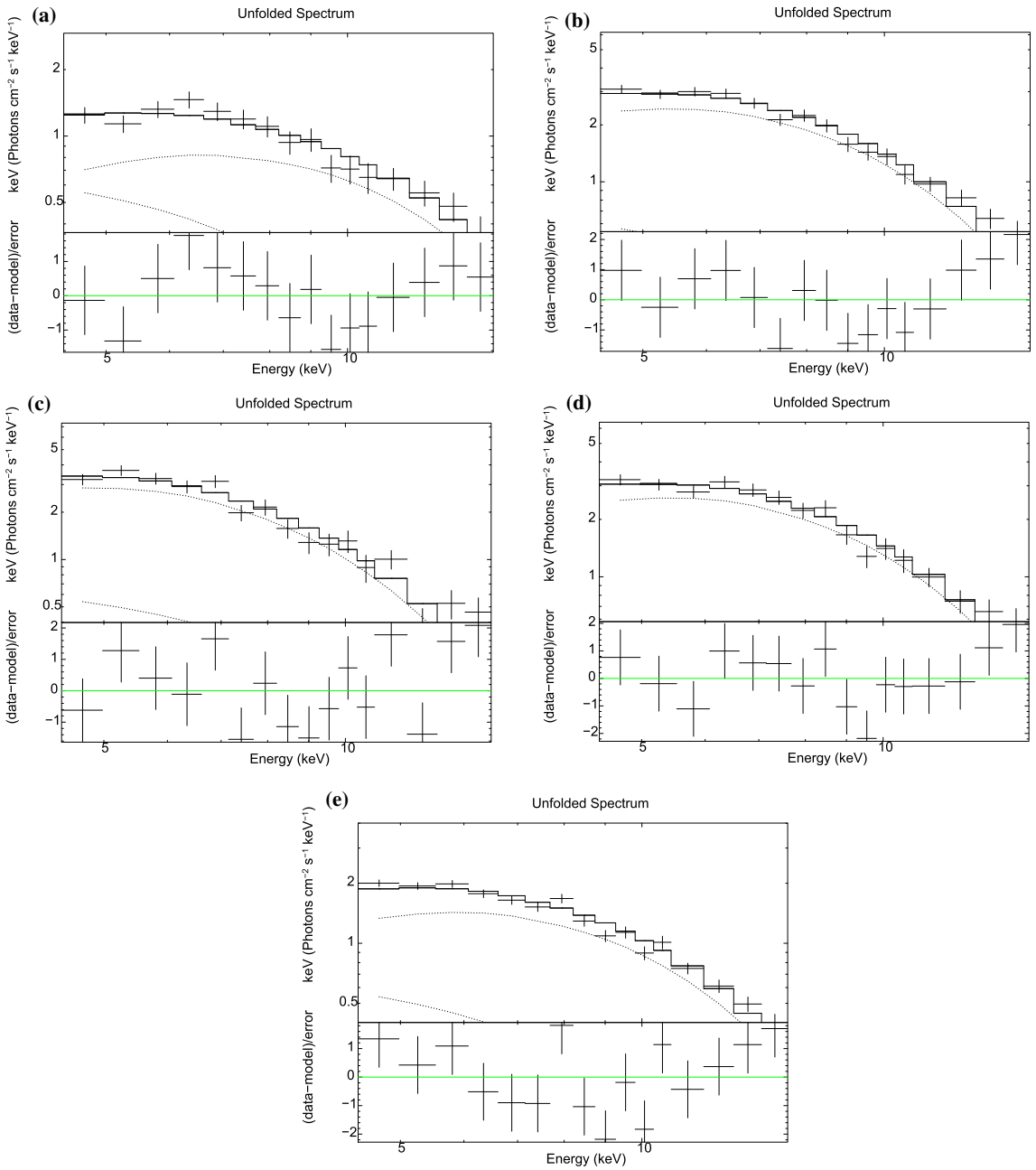

Figure 9. Time resolved spectroscopy of the burst using five time bins. We modeled the spectra during rise T1 shown by Figure (a); Figures (b), (c), (d) and (e) are the unfolded modeled spectra corresponding to the time bins T2, T3, T4 and T5. Each of the spectra is fitted following the conventional method on TBABS × (NTHCOMP + BBODYRAD). NTHCOMP parameters are frozen at pre-burst values for all the spectra.

Table 3. The best-fit parameters of BBODYRAD achieved during time-resolved spectroscopy of the burst. The model fitted is TBABS × (NTHCOMP + BBODYRAD). The parameter values of TBABS and NTHCOMP are kept frozen to the values achieved during modeling of the pre-burst emission. The energy band taken here for all the time bins is 4.0–16.0 keV. All the errors are at 90% confidence range.

	BBODYRAD				
Parameter	T1	T2	T3	T4	T5
kT_{bb}^{α}	$2.30^{+0.16}_{-0.14}$	$1.84^{+0.06}_{-0.06}$	$1.61^{+0.08}_{-0.08}$	$1.83^{+0.07}_{-0.07}$	$2.0^{+0.06}_{-0.06}$
Norm_{bb}^{β}	$46.82^{+14.13}_{-11.10}$	$269.42^{+44.8}_{-38.3}$	$496.05^{+138.64}_{-106.98}$	$301.40^{+60.7}_{-50.51}$	$124.78^{+17.18}_{-15.09}$
Radius^{γ}	$4.16^{+0.60}_{-0.47}$	$9.43^{+0.88}_{-0.75}$	$13.58^{+1.89}_{-1.46}$	$10.6^{+1.06}_{-0.88}$	$6.81^{+0.46}_{-0.41}$
χ^2/d.o.f	0.81	1.16	1.65	1.12	1.67
Flux^{δ}	$1.12^{+0.15}_{-0.15}$	$2.58^{+0.24}_{-0.24}$	$2.54^{+0.23}_{-0.23}$	$2.76^{+0.26}_{-0.26}$	$1.67^{+0.1}_{-0.1}$

$^{\alpha}$Blackbody temperature in keV units. $^{\beta}$Normalization constant of BBODYRAD is given by $\text{Norm}_{bb} = R^2/D^2_{10\text{ kpc}}$, where R is the radius in km and $D_{10\text{ kpc}}$ is the source distance in units of 10 kpc. $^{\gamma}$Radius of the photosphere in units of km, estimated for a source distance of 6.1 kpc. $^{\delta}$Unabsorbed blackbody flux in 10^{-8} ergs s^{-1} cm^{-2} units

blackbody temperature rises again following a drop in the normalization value. We could also observe that the unabsorbed flux is nearly constant from time bin T2 to T4 (the time interval during which the burst has shown the double peak at higher energies). We highlight that at T2, the Norm_{bb} is obtained with an almost six fold increase from T1. The normalization values are used to estimate the radius using the relation[5] $\text{Norm}_{bb} = R^2/D^2_{10\text{ kpc}}$ and we achieve the maximum value of the photospheric radius $13.58^{+1.89}_{-1.46}$ km, which agrees with the inner disk radius reported by Mondal *et al.* (2019) using NuSTAR data, in which they have also mentioned an upper limit of ≤13 km to the NS radius. To showcase all these parametric changes involved during the burst span, we have plotted the physical parameters vs time with $t = 0$ as the burst rise in Figure 10. We have not used any color correction factor to derive the radius and the burst temperature. The radii values are estimated for a source distance of 6.1 kpc (Kuulkers & van der Klis 2000) reported for a helium-rich photosphere.

5. Discussion and conclusions

In this work, we report the AstroSat observation of the bright atoll source, the LMXB GX 3+1. The light curve obtained from LAXPC 20 instrument indicated the presence of a thermonuclear burst feature of type-I. Our temporal analysis revealed that the instrument SXT had observed the source simultaneously with the LAXPC 20 during the pre-burst stage till ∼ 2 min before the burst was detected by LAXPC 20. Since LAXPC is operational during both orbital day and night and SXT can only observe during orbital night, there is more exposure by LAXPC than SXT prior to the satellite entering the South Atlantic Anomaly (SAA) passage. Hence, unfortunately, SXT data is not available during the thermonuclear burst.

It is noteworthy that the large collective area of LAXPC has allowed us to generate an energy-resolved burst profile and we have followed Beri *et al.* (2019) and Bhulla *et al.* (2020). A drop in count rate in the light curve of the X-ray burst is observed when the narrow energy bands become harder. Also, we found that the burst was the brightest in 5–8 keV energy band with a count rate higher than the softest band 3–5 keV. From our QDP modeling, we found that the burst decays faster at higher energies, which indicates that the temperature is decreasing as the burst evolves. This trend is similar to the behavior of the burst from 4U 1636-536, an atoll source, reported by Beri *et al.* (2019). We also noticed a double-peak feature in the burst at higher energies, i.e., 8–12 and 12–20 keV. This is a quick event ∼2 s within which the burst had showed the double peak, indicating a radius expansion phase (Paczynski 1983; Watts and Maurer 2007). It is necessary to highlight that double-peak bursts are also observed for bursts categorized as non-PRE bursts (Regev and Livio 1984), where the double peak feature is observed for low energies as well, theoretically modeled by Fujimoto *et al.* (1988), Melia and Zylstra (1992), Fisker *et al.* (2004), Bhattacharyya & Strohmayer (2006), Zhang *et al.* (2009), Lampe *et al.* (2016) and Bult *et al.* (2019).

[5] https://heasarc.gsfc.nasa.gov/xanadu/xspec/manual/node137.html.

We now discuss about our modeling of the pre-burst or persistent spectra. The seed photon temperature is found to be <1 keV in the literature reports of GX 3+1, but Pintore *et al.* (2015) has obtained values ≥1 keV for their two used models, both involving the thermally Comptonized NTHCOMP without fixing the seed photon temperature with the disk blackbody temperature. In our case, the persistent pre-burst spectrum is fitted by an NTHCOMP for a disk blackbody emission and without any explicit DISKBB (Makishima *et al.* 1983; Mitsuda *et al.* 1984). The $kT_{\rm nth}$ is obtained to be >1.8 keV. This is in close agreement to inner disk temperature reported by Mondal *et al.* (2019). We mention that the atoll source 4U 1728-34 is reported with seed photons >1.6 keV by Bhattacharyya *et al.* (2018) for an NTHCOMP model with disk blackbody as input (no explicit disk blackbody component is used). We also mention that we could not improve the fitting of the pre-burst spectra by adding DISKBB or BBODY models to NTHCOMP. Since we have used the NTHCOMP model only to model the pre-burst spectrum, where blackbody seed photons were not the input, the Comptonizing layer must have primarily covered the disk (Bhattacharyya *et al.* 2018).

During the spectral modeling of the burst, we have used the model BBODYRAD, which directly leads to estimate the radius of the source. We found that the photopshere shrinks and the radius reaches to a value of ∼6.81 km during the decay of the burst. Bhattacharyya *et al.* (2018) systematically examined the relative differences in the blackbody normalization values achieved for both the conventional and the f_a method, and the latter has been found to provide lower normalization values and hence, a smaller NS radius. We have also tried adopting the f_a methodology to model burst spectra, but the data quality is not good enough to constrain complex models. Referring to Figure 10, we see that the photospheric radius increases and reaches a local maximum at the same time when the blackbody temperature kT_{bb} reaches the minimum value as it could be seen at the top plot. From T2 to almost T4, which describes the PRE episode, the unabsorbed X-ray flux is found to remain approximately constant at ∼(2.58–2.76 in 10^{-8} ergs s^{-1} cm^{-2}), which is expected for a PRE burst (Strohmayer & Bildsten 2006; Galloway *et al.* 2008). During the double-peak event, the source contracts and the photosphere expands thus, the flux and hence, the luminosity is expected to remain almost constant. This is derived from the understanding that luminosity is directly dependent to both the source temperature and the radius. The expansion of the photosphere leads to a drop in photon temperature and thus, X-ray count rate

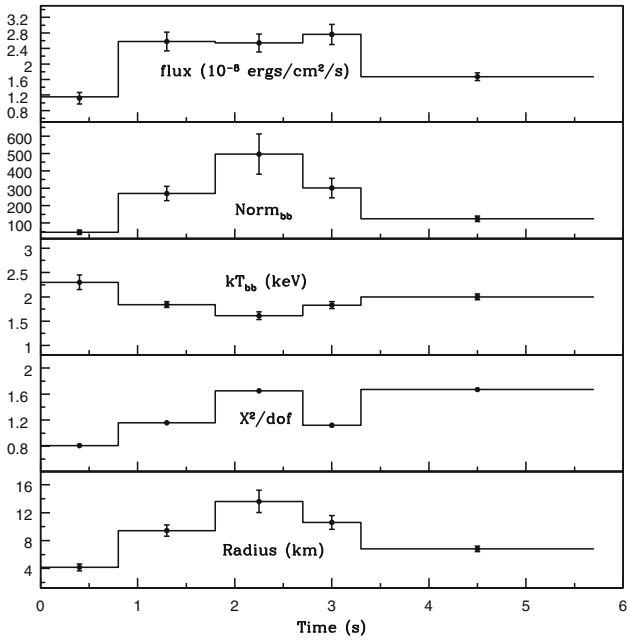

Figure 10. A combined plot of the evolution of unabsorbed flux, the normalization constant of blackbody model, blackbody temperature kT_{bb}, the model error and the estimated photospheric radius in km for a source distance of 6.1 kpc. The x-axis counts the time from the rise of the burst.

drops (Tawara *et al.* 1984). Studies performed using the BeppoSAX data by Beri *et al.* (2016) indicated the presence of high temperatures (∼3 keV) for X-ray bursts showing double-peaked profiles at higher energies, however, we do not find the presence of such high temperatures during the touchdown period. Since we have used a frozen pre-burst model as a background to the burst spectra, hence, we are unable to investigate the effect of burst on the persistent emissions during the PRE event, which was previously carried out for a non-PRE burst by Bhattacharyya *et al.* (2018).

It is worthy to mention that during the years 1983–2006, most of the reports of bursts from GX 3+1 had been published, after which no burst event is reported for almost more than a decade. As mentioned in our Introduction section (Section 1), the first measurement of the radius of the NS was carried out by Kuulkers & van der Klis (2000) and the authors have reported a radius of 4.5 ± 0.3 km during the non-burst period. This is consistent with the radius value derived by us during T1 (rise of the burst, see Figure 10) $\sim 4.16 \pm 0.53$ km. A single blackbody approximation on burst spectrum modeled by Molkov *et al.* (1999) had reported the NS radius to be 7.2 ± 1.2 km for a considered source distance of 8.5 kpc. If we consider a source distance of 8.5 kpc, we obtain the touchdown radius to be ∼9.5 km. In addition, the estimation of source distance could be well

derived during a PRE, and ever since Kuulkers & van der Klis (2000) had reported it, the source distance has not been calculated with a greater precision. Since, we could detect a PRE event, we attempt to estimate the source distance. The peak luminosity during the PRE event is considered to reach the source's Eddington luminosity, as the NS surface is lifted up. We use this opportunity to estimate the source distance by using the peak flux obtained by us from Table 3. The peak photon flux (F_b) is related to the Eddington luminosity ($L_{\rm Edd}$) by a linear equation, which is the modified Stefan–Boltzmann law for an LMXB, given by Lewin *et al.* (1993):

$$L_{\rm Edd} = 4\pi d^2 \xi_b F_b. \quad (1)$$

Here, we have assumed the anisotropy constant ξ_b to be unity, which corresponds to the isotropic case. The subscript b stands for burst. Keeping this equation in mind, we proceed towards deriving the Eddington luminosity from the equation (Pike *et al.* 2021)

$$L_{\rm Edd} = \frac{4\pi cGM}{\kappa_0}\left[1 - \frac{2GM}{c^2 \rm R}\right]^{1/2} \times \left[1 + \left(\frac{kT}{39.2\ \rm keV}\right)^{0.86}\right](1+X)^{-1}, \quad (2)$$

where M is the mass of the NS, G is the gravitational constant and c is the speed of light. We have assumed a typical NS mass of 1.4 $M_\odot$. We have considered the hydrogen mass fraction $X = 0$ and the typical upper limit of the NS radius as $R = 10$ km. We use the value of $\kappa_0 = 0.2\ \rm cm^2\ g^{-1}$, which is the opacity factor for pure He (Pike *et al.* 2021). Using the value of kT_{bb} for the T4 time bin of Table 3, we found the value of Eddington luminosity $L_{\rm Edd} = 2.87 \times 10^{38}$ erg s^{-1}. Substituting this value of luminosity and choosing the value of F_b as the highest flux value from Table 3, which corresponds to the T4 time bin in Equation (1), we achieve the distance $d = 9.3 \pm 0.4$ kpc. For a range of $0.5 < \xi_b < 2$ (Kuulkers & van der Klis 2000), we obtain d in the range of 6.6–13.2 kpc. We believe that to obtain source's physical parameters with greater accuracy, a refinement in the spectral analysis is required on a better data.

Acknowledgements

This report work has utilized the softwares provided by the High Energy Astrophysics Science Archive Research Centre (HEASARC). The authors AN and BS acknowledge the financial support of ISRO under AstroSat archival Data utilization program (no. DS_2B-13013(2)/2/2019-Sec.2). This publication uses data from the AstroSat mission of the Indian Space Research Organization (ISRO), archived at the Indian Space Science Data Centre (ISSDC). AN acknowledges the Inter-University Center for Astronomy and Astrophysics (IUCAA), Pune, for the periodic visits, the hospitality and the facilities provided to him to make possible the major part of the work. This work has been performed utilizing the calibration data bases and auxillary analysis tools developed, maintained and distributed by AstroSat–SXT team with members from various institutions in India and abroad. This research has made use of MAXI data provided by RIKEN, JAXA and the MAXI team (Matsuoka *et al.* 2009). BS also acknowledges the visiting associateship program at IUCAA and is grateful to IUCAA for hospitality during his visits, where part of this work was done. AN thanks Dr M. Pahari, Royal Society SERB International Fellow for his useful suggestions in this work. AN personally thanks the scholar mates from Jamia Millia Islamia University, Delhi, and other fellow mates who helped him to resolve issues faced in this work. BS would like to acknowledge discussions held with Dr Anjali Rao during the initial stages of this work. Authors are also indebted to the reviewer for providing beneficial suggestions and constructive comments, which has greatly enhanced the quality of the work.

References

Alizai K., Chenevez J., Brandt S., *et al.* 2020, MNRAS, 494, 2509
Antia H. M., Yadav J. S., Agrawal P. C., *et al.* 2017, ApJS, 231, 10
Antia H. M., Agrawal P. C., Dedhia D., *et al.* 2021, JoAA, 42, 32
Arnaud K. A. 1996, ADASS V, 101, 17
Asai K., Dotani T., Nagase F., *et al.* 1993, PASJ, 45, 801
Beri A., Paul B., Orlandini M., *et al.* 2016, New Ast., 45, 48. https://doi.org/10.1016/j.newast.2015.10.013
Beri A., Paul B., Yadav J. S., *et al.* 2019, MNRAS, 482, 4397
Belian R. D., Connor J. P., Evans W. D. 1976, IAU Circ., 1, 2969
Bhattacharya D., van den Heuvel E. P. J. 1991, PhR, 203, 1
Bhattacharyya S., Strohmayer T. E. 2006, ApJL, 636, L121
Bhattacharyya S. 2010, Advances in Space Research, 45, 949
Bhattacharyya S., Yadav J. S., Sridhar N., *et al.* 2018, ApJ, 860, 88
Bhattacharyya S., Singh K. P., Stewart G., *et al.* 2021, JoAA, 42, 17
Bhulla Y., Roy J., Jaaffrey S. N. A. 2020, Research in Astronomy and Astrophysics, 20, 098
Bowyer S., Byram E. T., Chubb T. A., *et al.* 1965, AnAp, 28, 791
Bradt H. V., Rothschild R. E., Swank J. H. 1993, A&AS, 97, 355

Bult P., Jaisawal G. K., Güver T., *et al*. 2019, ApJL, 885, L1
Chen Y.-P., Zhang S., Zhang S.-N., *et al.* 2012, ApJL, 752, L34
Chen Y. P., Zhang S., Zhang S. N., *et al.* 2019, Journal of High Energy Astrophysics, 24, 23
Chenevez J., Falanga M., Brandt S., *et al.* 2006, A&A, 449, L5
Degenaar N., Ballantyne D. R., Belloni T., *et al.* 2018, Space Sci. Rev., 214, 15
Degenaar N., Koljonen K. I. I., Chakrabarty D., *et al.* 2016, MNRAS, 456, 4256
den Hartog P. R., in't Zand J. J. M., Kuulkers E., *et al.* 2003, A&A, 400, 633
Devasia J., Raman G., Paul B. 2021, New Astron., 83, 101479
Fisker J. L., Thielemann F.-K., Wiescher M. 2004, ApJL, 608, L61
Fujimoto M. Y., Sztajno M., Lewin W. H. G., *et al*. 1988, A&A, 199, L9
Galloway D. K., Muno M. P., Hartman J. M., *et al*. 2008, ApJS, 179, 360
Galloway D. K., in't Zand J., Chenevez J., *et al.* 2020, ApJS, 249, 32
Grindlay J., Gursky H., Schnopper H., *et al.* 1976, ApJL, 205, L127
Homan J., van der Klis M., Wijnands R., *et al.* 1998, ApJL, 499, L41
Hoffman J. A., Lewin W. H. G., Doty J. 1977, ApJL, 217, L23
Hoffman J. A., Marshall H. L., Lewin W. H. G. 1978, Nature, 271, 630
Hu C.-P., Begiçarslan B., Güver T., *et al.* 2020, ApJ, 902, 1
in't Zand J. J. M., Galloway D. K., Marshall H. L., *et al*. 2013, A&A, 553, A83
Kashyap U., Chakraborty M., Bhattacharyya S. 2022a, MNRAS, 512, 6180
Kashyap U., Ram B., Güver T., *et al.* 2022b, MNRAS, 509, 3989
Keek L., Arzoumanian Z., Bult P., *et al.* 2018, ApJL, 855, L4
Kuulkers E. van der Klis M. 2000, A&A, 356, L45
Kuulkers E. 2002, A&A, 383, L5
Lampe N., Heger A., Galloway D. K. 2016, ApJ, 819, 46
Levine A. M., Bradt H., Cui W., *et al.* 1996, ApJL, 469, L33
Lewin W. H. G., van Paradijs J., Taam R. E. 1993, Space Sci. Rev, 62, 223
Ludlam R. M., Miller J. M., Barret D., *et al.* 2019, ApJ, 873, 99
Majumder S., Sreehari H., Aftab N., *et al.* 2022, MNRAS, 512, 2508
Makishima K., Mitsuda K., Inoue H., *et al.* 1983, ApJ, 267, 310
Maqbool B., Mudambi S. P., Misra R., *et al.* 2019, MNRAS, 486, 2964
Marino A., Del Santo M., Cocchi M., *et al.* 2019, MNRAS, 490, 2300
Matsuoka M., Kawasaki K., Ueno S., *et al.* 2009, PASJ, 61, 999
Melia F., Zylstra G. J. 1992, ApJL, 398, L53
Misra R., Yadav J. S., Verdhan Chauhan J., *et al.* 2017, ApJ, 835, 195
Mitsuda K., Inoue H., Koyama K., *et al.* 1984, PASJ, 36, 741
Molkov S. V., Grebenev S. A., Pavlinsky M. N., *et al.* 1999, Astrophysical Letters and Communications, 38, 141
Mondal A. S., Dewangan G. C., Raychaudhuri B. 2019, MNRAS, 487, 5441
Morrison R., McCammon D. 1983, ApJ, 270, 119
Mudambi S. P., Maqbool B., Misra R., *et al.* 2020, ApJL, 889, L17
Oosterbroek T., Barret D., Guainazzi M., *et al.* 2001, A&A, 366, 138
Paczynski B. 1983, ApJ, 267, 315
Paizis A., Farinelli R., Titarchuk L., *et al.* 2006, A&A, 459, 187
Pavlinsky M. N., Grebenev S. A., Sunyaev R. A. 1994, ApJ, 425, 110
Pike S. N., Harrison F. A., Tomsick J. A., *et al.* 2021, ApJ, 918, 9
Pintore F., Di Salvo T., Bozzo E., *et al.* 2015, MNRAS, 450, 2016
Regev O., Livio M. 1984, A&A, 134, 123
Roy P., Beri A., Bhattacharyya S. 2021, MNRAS, 508, 2123
Schulz N. S., Hasinger G., Truemper J. 1989, A&A, 225, 48
Seifina E., Titarchuk L. 2012, ApJ, 747, 99
Singh K. P., Stewart G. C., Chandra S., *et al.* 2016, Proc. SPIE, 9905, 99051E
Singh K. P., Stewart G. C., Westergaard N. J., *et al.* 2017, JoAA, 38, 29
Sreehari H., Ravishankar B. T., Iyer N., *et al.* 2019, MNRAS, 487, 928
Sreehari H., Nandi A., Das S., *et al.* 2020, MNRAS, 499, 5891
Strohmayer T., Bildsten L. 2006, Compact Stellar X-ray sources, p. 113
Swank J. H., Becker R. H., Boldt E. A., *et al.* 1977, ApJL, 212, L73
Tawara Y., Kii T., Hayakawa S., *et al.* 1984, ApJL, 276, L41
van den Berg M., Homan J., Fridriksson J. K., *et al.* 2014, ApJ, 793, 128
Verdhan Chauhan J., Yadav J. S., Misra R., *et al.* 2017, ApJ, 841, 41
Verbunt F. 1993, ARAA, 31, 93
Watts A. L., Maurer I. 2007, A&A, 467, L33
Wilms J., Allen A., McCray R. 2000, ApJ, 542, 914
Worpel H., Galloway D. K., Price D. J. 2013, ApJ, 772, 94
Worpel H., Galloway D. K., Price D. J. 2015, ApJ, 801, 60
Yadav J. S., Misra R., Verdhan Chauhan J., *et al.* 2016, ApJ, 833, 27
Zdziarski A. A., Johnson W. N., Magdziarz P. 1996, MNRAS, 283, 193
Zhang G., Méndez M., Altamirano D., *et al.* 2009, MNRAS, 398, 368
Życki P. T., Done C., Smith D. A. 1999, MNRAS, 309, 561